

# ALMA Observations of Giant Molecular Clouds in M33 I: Resolving Star Formation Activities in the Giant Molecular Filaments Possibly Formed by a Spiral Shock

KAZUKI TOKUDA,<sup>1,2</sup> KAZUYUKI MURAOKA,<sup>1</sup> HIROSHI KONDO,<sup>1</sup> ATSUSHI NISHIMURA,<sup>1</sup> TOMOKA TOSAKI,<sup>3</sup>  
SAROLTA ZAHORECZ,<sup>1,2</sup> SACHIKO ONODERA,<sup>4</sup> RIE E. MIURA,<sup>2</sup> KAZUFUMI TORII,<sup>5</sup> NARIO KUNO,<sup>6,7</sup> SHINJI FUJITA,<sup>1</sup>  
HIDETOSHI SANO,<sup>8,9</sup> TOSHIKAZU ONISHI,<sup>1</sup> KAZUYA SAIGO,<sup>2</sup> YASUO FUKUI,<sup>8,9</sup> AKIKO KAWAMURA,<sup>2</sup> AND KENGO TACHIHARA<sup>8</sup>

<sup>1</sup>*Department of Physical Science, Graduate School of Science, Osaka Prefecture University, 1-1 Gakuen-cho, Naka-ku, Sakai, Osaka 599-8531, Japan*

<sup>2</sup>*National Astronomical Observatory of Japan, National Institutes of Natural Science, 2-21-1 Osawa, Mitaka, Tokyo 181-8588, Japan*

<sup>3</sup>*Joetsu University of Education, Yamayashiki-machi, Joetsu, Niigata 943-8512, Japan*

<sup>4</sup>*Meisei University, 2-1-1 Hodokubo, Hino, Tokyo 191-0042, Japan*

<sup>5</sup>*Nobeyama Radio Observatory, National Astronomical Observatory of Japan (NAOJ), National Institutes of Natural Sciences (NINS), 462-2 Nobeyama, Minamimaki, Minamisaku-gun, Nagano 384-1305, Japan*

<sup>6</sup>*Department of Physics, Graduate School of Pure and Applied Sciences, University of Tsukuba, 1-1-1 Tennodai, Tsukuba, Ibaraki 305-8577, Japan*

<sup>7</sup>*Tomonaga Center for the History of the Universe, University of Tsukuba, Tsukuba, Ibaraki 305-8571, Japan*

<sup>8</sup>*Department of Physics, Nagoya University, Chikusa-ku, Nagoya 464-8602, Japan*

<sup>9</sup>*Institute for Advanced Research, Nagoya University, Furo-cho, Chikusa-ku, Nagoya 464-8601, Japan*

(Received; Revised; Accepted)

Submitted to ApJ

## ABSTRACT

We report molecular line and continuum observations toward one of the most massive giant molecular clouds (GMCs), GMC-16, in M33 using ALMA with an angular resolution of  $0''.44 \times 0''.27$  ( $\sim 2 \text{ pc} \times 1 \text{ pc}$ ). We have found that the GMC is composed of several filamentary structures in  $^{12}\text{CO}$  and  $^{13}\text{CO}$  ( $J=2-1$ ). The typical length, width, and total mass are  $\sim 50-70 \text{ pc}$ ,  $\sim 5-6 \text{ pc}$ , and  $\sim 10^5 M_{\odot}$ , respectively, which are consistent with those of giant molecular filaments (GMFs) as seen in the Galactic GMCs. The elongations of the GMFs are roughly perpendicular to the direction of the galaxy's rotation, and several H II regions are located at the downstream side relative to the filaments with an offset of  $\sim 10-20 \text{ pc}$ . These observational results indicate that the GMFs are considered to be produced by a galactic spiral shock. The 1.3 mm continuum and  $\text{C}^{18}\text{O}$  ( $J=2-1$ ) observations detected a dense clump with the size of  $\sim 2 \text{ pc}$  at the intersection of several filamentary clouds, which is referred to as “hub filament,” possibly formed by a cloud–cloud collision. A strong candidate for protostellar outflow in M33 also has been identified at the center of the clump. We have successfully resolved the pc-scale local star formation activity in which the galactic scale kinematics may induce the formation of the parental filamentary clouds.

**Keywords:** stars: formation — stars: protostars — ISM: clouds — ISM: kinematics and dynamics — ISM: individual (M33-GMC-16) — galaxies: Local Group

## 1. INTRODUCTION

Giant molecular clouds (GMCs) are considered to be major sites of high-mass star-formation (e.g., Heyer, & Dame 2015), and the formed stars eventually regulate the galaxy evolution through their feedback. Understanding of the physical properties of GMCs and their evolution is a challenging study observationally. The sizes of GMCs are as

large as  $>10\text{--}100\text{ pc}$ , and a large number of samples are needed to track the continuous evolution. Several comprehensive molecular gas surveys have been carried out toward the Local Group of galaxies, such as the Large Magellanic Cloud (LMC) (e.g., Fukui et al. 1999; Kawamura et al. 2009; Wong et al. 2011) and M33 (e.g., Miura et al. 2012; Corbelli et al. 2017). They classified the GMCs into a few groups with different evolutionary stages based on the association of H II regions and young massive star clusters, and then estimated the GMC lifetime as a few  $\times 10\text{ Myr}$ .

Star formation and GMC evolution in the spiral arm are classically considered to be controlled by galactic shock (Fujimoto 1968; Roberts 1969; Shu et al. 1973) caused by “quasi-stationary density waves” (e.g., Lin, & Shu 1964). In contrast to this, an alternative model called “dynamic” spiral theory, which involves non-steady stellar arms, has been proposed (Dobbs, & Baba (2014) and references therein). The two models predict qualitatively different gas distributions on the spiral arm. The former produces an apparent offset between parental gas and H II regions, but the latter does not show a clear spatial offset between them (Wada et al. 2011). Although recent observations toward grand-design spiral galaxies sometimes prefer to show a sequential distribution of gas and high-mass stars across spiral arm predicted by galactic shock (e.g., Egusa et al. 2004, 2011; Hirota et al. 2011; Colombo et al. 2014), the actual mechanism to trigger the star formation in the spiral arm is not well constrained by available observations. On spiral arms in galaxies, gas is exposed to many processes in addition to spiral shocks, such as cloud–cloud collision, hydrodynamic instabilities, stellar feedback, and self-gravity (see the review by Dobbs, & Baba 2014). In order to understand the mechanism driving GMC and high-mass star formation in spiral arms, it is important to reveal a high-dynamic-range picture from the galactic scale down to filaments/clumps (see the next paragraph) directly leading to star formation.

Molecular gas surveys using CO and its isotopes toward star-forming regions in the solar neighborhood, such as Taurus, revealed that filamentary structures are considered to be fundamental ingredients of molecular clouds (e.g., Mizuno et al. 1995; Onishi et al. 1996; Goldsmith et al. 2008; Hacar et al. 2013) and eventually collapse into individual dense cores and protostars. Recent high-resolution dust continuum observations with the *Herschel* telescope confirmed the quasi-universality of the filamentary structure in molecular clouds extending to the Galactic plane (André et al. 2014 and references therein), and the typical width of the filaments were measured as  $\sim 0.1\text{ pc}$  (Arzoumanian et al. 2011, 2019; André et al. 2016). Although the typical length of the above-mentioned filaments in the solar-neighborhood star-forming regions are  $\sim 10\text{ pc}$  or less, the observations toward the Galactic plane identify much longer filamentary complexes with the length scale of  $\gtrsim 50\text{--}100\text{ pc}$ , called “giant molecular filaments (GMFs).” One of the most prominent examples is the “Nessie” Nebula (Jackson et al. 2010), which is an infrared dark cloud on the Galactic plane. The long filamentary structure possibly formed by the passage of a spiral shock. One of the most active high-mass star-forming molecular complexes in the Galaxy, W51, also has a long filamentary stream with a length of  $\sim 100\text{ pc}$  (e.g., Burton, & Shane 1970; Moon, & Park 1998; Okumura et al. 2001; Fujita et al. 2019). The velocity of this stream is different from that of the main complex of W51, and this excess of the velocity may be due to the streaming motions induced by a spiral density-wave (Burton, & Shane 1970; Koo 1999). However, the actual origin of these GMFs/streamer may be hard to understand due to the serious contaminations at the line-of-sight in the Galactic plane and its edge-on view.

ALMA observations with an angular resolution of  $0''.25$  ( $\sim 0.06\text{ pc}$ ) toward GMCs in the LMC have started to resolve  $\sim 0.1\text{ pc}$  width molecular filaments (Fukui et al. 2019; Tokuda et al. 2019), possibly formed by a galactic-scale gas flow. Moderate resolution ( $\sim 3'' = 0.7\text{ pc}$ ) studies in the LMC also provided us hints for understanding the evolution of internal structures of GMCs. For example, Sawada et al. (2018) suggest that the quiescent GMC shows a diffuse emission, whereas the active star-forming ones have highly structured distributions, i.e., filaments and clumps. Wong et al. (2019) measured the linewidth-size relation in several GMCs down to  $\lesssim 1\text{ pc}$  and show the velocity dispersion at a fixed size slightly increases as star formation progresses.

The early mm/sub-mm observations described in this section suggest that we need at least  $\sim 1\text{ pc}$  resolution to understand the internal gas properties of molecular clouds and their kinematics. In addition to this, a birds-eye view is needed to understand the relation between spiral arms and local star formation activities. One of the closest galaxies, the LMC and Small Magellanic Cloud, are not the best targets in this purpose because the irregular galaxies do not have clear spiral arms. The flocculent spiral galaxy M33 is almost a unique candidate so far to investigate the effect of the spiral arms on molecular cloud and high-mass star formation at a pc-scale resolution using ALMA thanks to its proximity ( $\sim 840\text{ kpc}$ ; Freedman et al. 2001) and favorable inclination ( $i = 51\text{ degree}$ ; Corbelli & Salucci 2000).

We have performed ALMA observations with a spatial resolution of  $\sim 2\text{ pc} \times 1\text{ pc}$  toward three massive ( $\sim 10^6 M_\odot$ ) GMCs (NGC 604-GMC, GMC-8, and GMC-16) in different evolutionary stages identified by the early surveys

(Rosolowsky et al. 2007; Onodera et al. 2010; Miura et al. 2012) to investigate the molecular gas structures and star-formation activities. In this paper, we present the results of GMC-16 associated with several H II regions and 24  $\mu\text{m}$  sources (Verley et al. 2007). We note that CO (3–2) observations of M33 by Miura et al. (2012) cataloged the present target as two clouds, GMC-2 and GMC-16, which correspond to the cloud number of 425 and 435 in Corbelli et al. (2017), respectively. Because the two clouds spatially connect each other, we treat these objects as a single molecular cloud system for convenience throughout the manuscript and use the name of GMC-16 as a representative, which is more luminous in CO (3–2) than the other. We describe the detailed results of the other targets in a separate paper for NGC 604-GMC (K., Muraoka et al. 2020 in prep.) and a forthcoming paper for GMC-8.

## 2. OBSERVATIONS

We performed ALMA Cycle 5 Band 6 (1.3 mm) observations in molecular lines and continuum toward three GMCs in M33 (P.I.: K., Muraoka, #2017.1.00461.S). We used the ALMA main array (the 12 m array) with the configuration of C43-5 as well as the 7 m array of the Atacama Compact Array (ACA; a.k.a. Morita Array). The observations were carried out during 2017 October and 2018 October. There were three spectral windows targeting  $^{12}\text{CO}$  ( $J=2-1$ ),  $^{13}\text{CO}$  ( $J=2-1$ ), and  $\text{C}^{18}\text{O}$  ( $J=2-1$ ). The bandwidths of the correlator setting were 117.19 MHz with 1920 channels for  $^{12}\text{CO}$  and 960 channels for  $^{13}\text{CO}/\text{C}^{18}\text{O}$ . We used two spectral windows for the continuum observations with an aggregate bandwidth of 3750 MHz with a channel width of 0.98 MHz.

While we did not change the system calibration provided by the observatory, the data was re-processed with the Common Astronomy Software Application (CASA) package (McMullin et al. 2007) version 5.4.0 in the imaging process. We used the `tclean` task with the `multi-scale` deconvolver. We applied the briggs weighting with a robust parameter of 0.5 and the natural weighting to the 12 m and 7 m array data, respectively. We used the `auto-multithresh` procedure (Kepley et al. 2020) in `tclean` to select the emission mask in the dirty and residual images. We continued the deconvolution process until the intensity of the residual image reached  $\sim 1\sigma$  noise level. We combined the individually imaged 12 m and 7 m array data sets with the `feathering` task. We also performed the multiple array data combination with an alternative method, in which the visibility data of the 12 m and 7 m array were merged together before the `tclean` task, and then imaged them using the same auto-masking technique as described above. The two different methods fairly reproduce similar results (only  $\lesssim 10\%$  flux difference in r.m.s.), and we used the first option in the analysis through the manuscript.

The final processed image qualities are summarized as follows. The beam sizes of the molecular lines ( $^{12}\text{CO}$ ,  $^{13}\text{CO}$ , and  $\text{C}^{18}\text{O}$ ) and continuum data are  $0''.44 \times 0''.27$ , corresponding to  $\sim 2\text{ pc} \times 1\text{ pc}$ , and  $0''.40 \times 0''.25$ , respectively. The rms noise levels of the molecular lines at a velocity resolution of  $\sim 0.2\text{ km s}^{-1}$  are  $\sim 4.3\text{ mJy beam}^{-1}$  ( $\sim 0.9\text{ K}$ ). The sensitivity of the continuum observations is  $\sim 0.02\text{ mJy beam}^{-1}$ .

We estimated the missing flux of the interferometric observations toward GMC-16 using the available  $^{12}\text{CO}$  ( $J=2-1$ ) data obtained with the single-dish IRAM 30 m telescope (Druard et al. 2014). We spatially smoothed the 12 m+7 m data to an angular resolution of  $12''$ , which is the same as the IRAM data and then compared the total flux between the two images. Since the total missing flux of the  $^{12}\text{CO}$  12 m+7 m data in the observed field (Figure 1 (a)) is  $\sim 40\%$ , we additionally combined the IRAM image with the ALMA data using the `feathering` technique, and we confirmed that the combined image reproduces the total flux measured with the IRAM data alone. We assume that the  $^{13}\text{CO}$ ,  $\text{C}^{18}\text{O}$ , and continuum observations have no significant missing flux, because the distributions of these tracers are more compact than those of  $^{12}\text{CO}$ .

We retrieved the SUBARU H $\alpha$  Supreme-cam image (PI: Arimoto, N.; Proposal IDs: S01B091, S02B105) from the archive and calibrated with a standard manner to investigate the star formation activities in the GMC (see Sect. 3.1). The absolute astrometry of the original H $\alpha$  image is  $\sim 0''.2$ , as we align the image using the UBNO-B1 catalog. To confirm the accuracy of the astrometry, a point source catalog of *Gaia* Data Release 2 (Bailer-Jones et al. 2018) was used, and thus there is no significant positional error of the H $\alpha$  image over the ALMA beam size.

## 3. RESULTS

### 3.1. Spatial Distributions of Molecular Gas of GMC-16

Figure 1 shows the molecular gas distributions in  $^{12}\text{CO}$  and  $^{13}\text{CO}$  ( $J=2-1$ ) in GMC-16. The missing flux of the 12 m+7 m data in  $^{12}\text{CO}$  toward the southern region where the declination angle is lower than  $+30^\circ 48' 50''$  is as small as 10%, indicating that the gas distributions are dominated by compact rather than the diffuse gas. This is consistent with an early result that active star-forming GMCs in the LMC are highly structured (Sawada et al. 2018).

The previous single-dish studies in CO lines by [Tosaki et al. \(2011\)](#), [Miura et al. \(2012\)](#), and [Druard et al. \(2014\)](#) marginally resolved this GMC into two peaks. The ALMA observations clearly reveal multiple filamentary structures with the length scale of  $\gtrsim 50$  pc elongated to the north-south direction. The filaments are not randomly distributed but exhibit ordered direction and there are roughly two main filamentary components (Filament A, and B) as indicated in Figure 1 (a). In addition to these filaments, there is a relatively “extended gas” (see the final paragraph of this subsection) and a dense clump associated with the 1.3 mm continuum emission (hereafter, MMS, milli-meter source) and multiple small filaments (see Sect. 3.2) at the southern part of the GMC. We estimated the total gas mass and relatively dense gas mass from the  $^{12}\text{CO}$  and  $^{13}\text{CO}$  data, respectively. The first one is derived from the  $^{12}\text{CO}$  data assuming the  $X_{\text{CO}}$  factor in M33,  $2.0 \times 10^{20} \text{ cm}^{-2} (\text{K km s}^{-1})^{-1}$  ([Rosolowsky et al. 2007](#)), and  $\text{CO}(2-1)/\text{CO}(1-0)$  ratio of 0.7 ([Tosaki et al. 2011](#); [Druard et al. 2014](#)). The mass of higher density regions traced by  $^{13}\text{CO}$  is estimated by the local thermodynamical equilibrium (LTE) calculation applying the excitation temperature derived from the  $^{12}\text{CO}$  data and the relative abundance of  $[\text{H}_2]/[^{13}\text{CO}]$  of  $1.4 \times 10^6$ , which is close to an intermediate value adapted in the Galaxy (e.g., [Freking et al. 1982](#)) and the LMC studies (e.g., [Fujii et al. 2014](#); [Fukui et al. 2019](#); [Tokuda et al. 2019](#)). The total mass ( $^{12}\text{CO}$  mass) and dense gas mass ( $^{13}\text{CO}$  mass) are  $8 \times 10^5 M_\odot$  and  $2 \times 10^5 M_\odot$ , respectively. The fraction of  $^{13}\text{CO}/^{12}\text{CO}$  mass is  $\sim 0.2$ , which is consistent with that in the Galactic plane ([Torii et al. 2019](#)). The total mass, median (FWHM) width, and length of Filament A/B in the  $^{12}\text{CO}$  map are measured to be  $\sim 1 \times 10^5 M_\odot$ ,  $\sim 5$ –6 pc, and  $\sim 50$ –70 pc, respectively. These characteristics are comparable to those of GMFs, e.g., the Nessie cloud ([Jackson et al. 2010](#)), in the Galaxy.

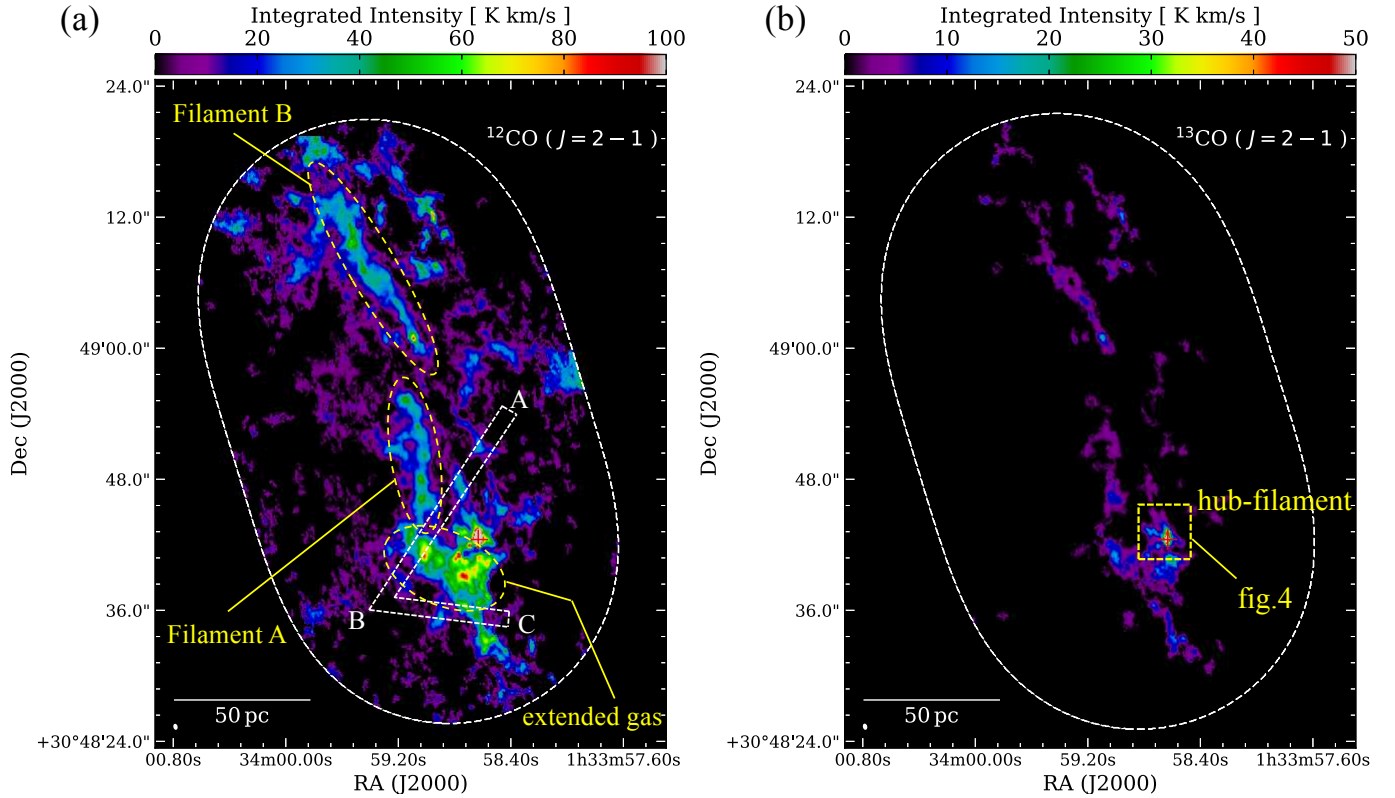


**Figure 1.** Molecular gas distributions in M33-GMC-16. (a) Color-scale image shows the velocity integrated intensity map of  $^{12}\text{CO}$  ( $J=2-1$ ) combining the ALMA data (the 12 m + 7 m array) with IRAM 30 m data. The angular resolution is given by the white ellipse in the lower left corner. The cross mark denotes the position of the 1.3 mm continuum peak. Note that the color scale is adjusted to the range from zero to  $100 \text{ K km s}^{-1}$  in order to show the diffuse emission and thus the CO peak is saturated in this figure. The white dotted line shows the field coverage of the ALMA observations. (b) Same as (a) but for the  $^{13}\text{CO}$  ( $J=2-1$ ) image obtained by the ALMA 12 m + 7 m array.

Figure 2 (a) shows that GMC-16 is located at an optical spiral arm in the northern part of M33. Based on the morphology of the spiral arm, the moving direction of the gas (i.e., galactic rotation) is considered to be from east to west. Figure 2 (b) shows the comparison between the  $^{12}\text{CO}$  and  $\text{H}\alpha$  images. There are several bright  $\text{H II}$  regions and



some of them is outside of the present field coverage with ALMA. Two GMFs (Filament A, and B) are located at the eastern side of the H II regions. Although the previous single-dish studies with a spatial resolution of a few  $\times 10$  pc identified these H II regions inside the molecular cloud, the present observations reveal a clear position offset between ionized and CO gas with a separation of  $\sim 10$ – $20$  pc.

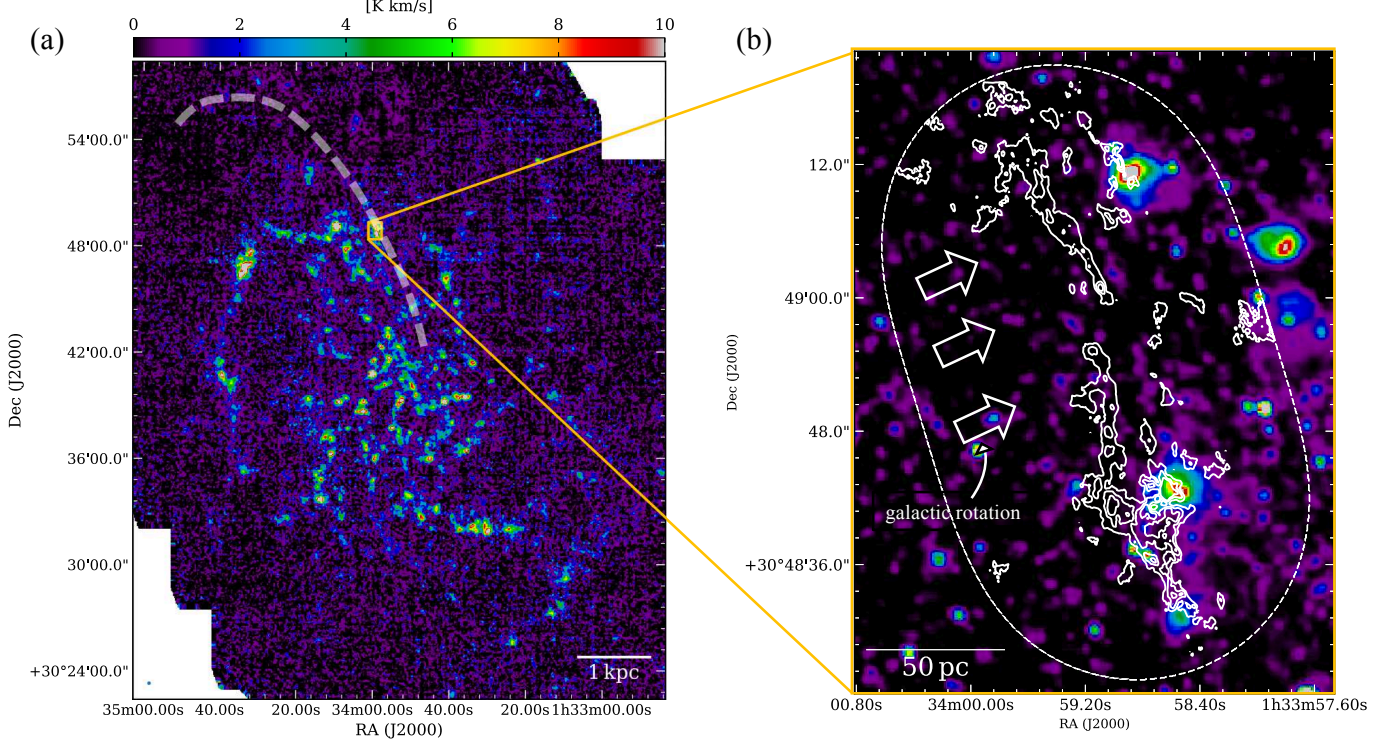


**Figure 2.** (a) The  $^{12}\text{CO}$  ( $J=2-1$ ) velocity-integrated intensity map of M33 obtained with the IRAM 30 m telescope (Druard et al. 2014). The transparent white dashed line indicate the optical arm near GMC-16 (Sandage, & Humphreys 1980). (b) Color-scale image shows H $\alpha$  emission obtained by the SUBARU telescope. Contour shows the  $^{12}\text{CO}$  map, which is the same as Figure 1 (a). The lowest contour level and the subsequent steps are  $20 \text{ K km s}^{-1}$ .

We made channel maps with a velocity bin of  $4 \text{ km s}^{-1}$  of the  $^{12}\text{CO}$  ( $J=2-1$ ) data to investigate the velocity structure of the GMC (Figure 3 (a)). As one can see in the channel maps, there is a velocity gradient along the north-south direction from blueshifted to redshifted velocity. To further illustrate the difference between the individual components, i.e., Filament A, extended gas, and some of the filaments, we made a position-velocity (PV) diagram of  $^{12}\text{CO}$  (Figure 3 (b)) along the dotted lines shown in Figure 1 (a). We manually selected the analyzed region to avoid the complex hub-filamentary structure (Sect. 3.2). The velocity width (FWHM) of the filamentary structures is measured as  $\sim 3 \text{ km s}^{-1}$ , in contrast to this, the extended gas shows much wider velocity width,  $\sim 6 \text{ km s}^{-1}$ . The centroid velocity of the extended gas is  $\sim -240 \text{ km s}^{-1}$ , which is apparently redshifted compared to that of Filament A. This differences may be relevant to turbulent dissipation and deceleration by the galactic spiral shock. We discuss this possibility in Sect. 4.1.

### 3.2. A compact millimeter source with high-velocity wing components in GMC-16

Figure 4 shows a zoom in view of the  $^{12}\text{CO}$  brightest peak clump in GMC-16. The panel (a) shows the  $^{13}\text{CO}$  distribution and there are several filamentary structures connecting to the central peak. This type of multiple filamentary structures, which is referred to as “hub filament” (Myers 2009), is found in high-mass star-forming regions in the Galaxy and the LMC (e.g., Peretto et al. 2013; Williams et al. 2018; Fukui et al. 2019; Tokuda et al. 2019). The hub filament in GMC-16 shows an asymmetric distribution, which is extended in a fan shape toward the east direction. The moment 1 map in Figure 4 (b) shows that the northern filament has a central velocity of  $\sim -248 \text{ km s}^{-1}$ , which is different from those of the other filaments ( $\sim -245 \text{ km s}^{-1}$ ). Note that the hub-filamentary complex is connected to the extended gas (see the moment 0 map (Figure 1) in Sect. 3.1), but their central velocities are different from each other.

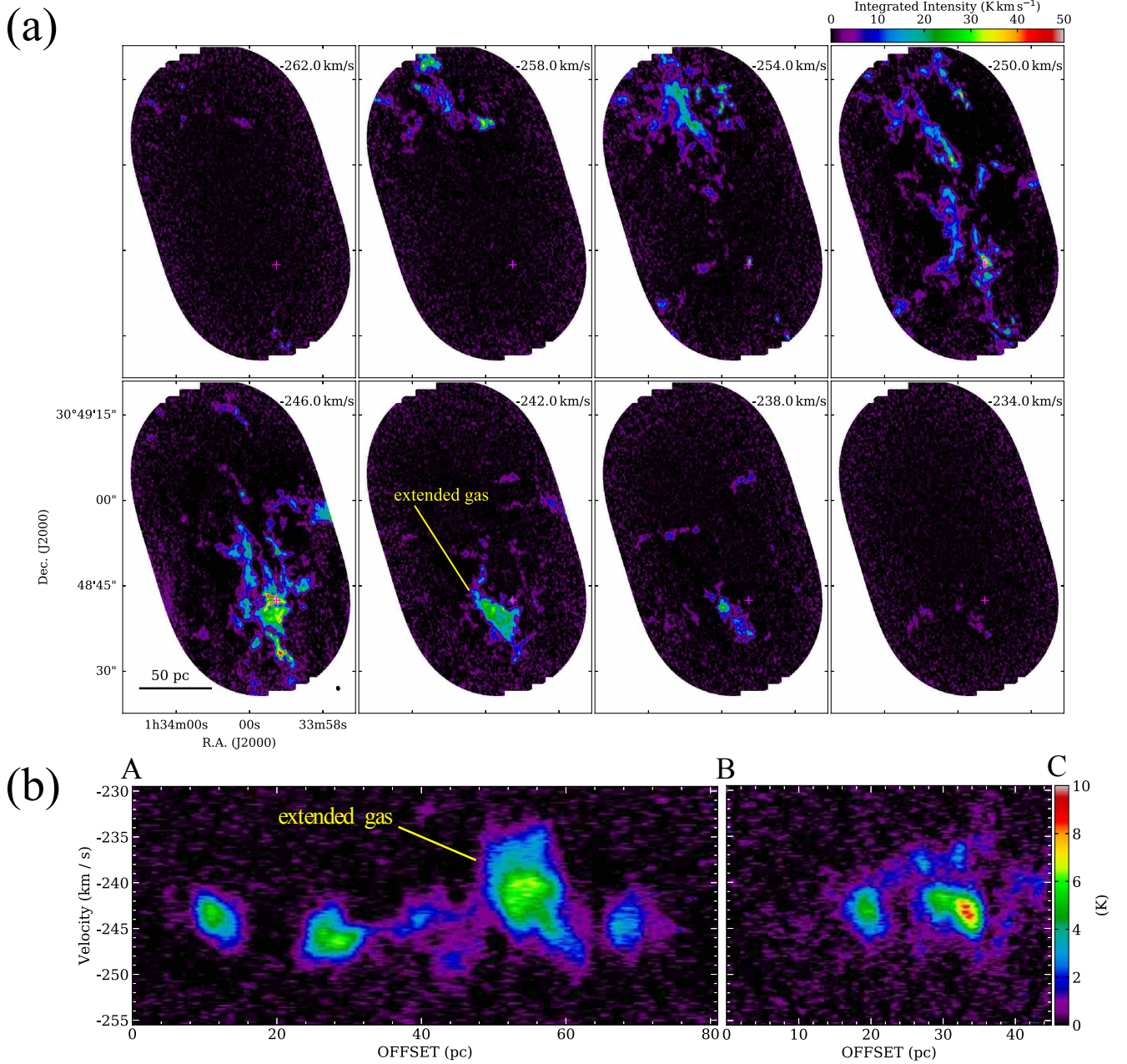


**Figure 3.** (a) Velocity-channel maps toward GMC-16 in  $^{12}\text{CO}$  ( $J=2-1$ ). The lowest velocities are shown in the upper right corners in each panel. The angular resolution is given by the black ellipse in the lower right corner of the lower left panel. (b) A  $^{12}\text{CO}$  ( $J=2-1$ ) position-velocity diagram along the regions shown by the white dotted lines through three positions, A, B, and C in the Figure 1 (a).

We detected the 1.3 mm continuum source (MMS) as well as the  $\text{C}^{18}\text{O}$  emission at the intersection of a few filaments, i.e., the  $^{13}\text{CO}$  peak (Figure 4 (a,d)). If there is a protostellar source inside MMS, the source may contribute to the enhancement of the 1.3 mm flux. This effect is considered to be small, and the continuum flux is mainly arising from the cold dust emission, because the gas mass estimated from the 1.3 mm continuum and that from the  $\text{C}^{18}\text{O}$  emission are similar to each other (see the next paragraph). For the same reason, it is likely that the free-free contamination from the  $\text{H II}$  region next to MMS is also negligible. In fact, the peak position of the hub filament as well as MMS is shifted from that of the  $\text{H}\alpha$  emission as shown in Figure 4 (c). The *Spitzer* observations found  $24\ \mu\text{m}$  emission



around this source with the intensity of 82 mJy, which corresponds to the total infrared luminosity of  $\sim 2 \times 10^6 L_\odot$  (Verley et al. 2007). Although the brightness of the source suggests the presence of early-O-type star(s) (Martins et al. 2005; Zinnecker & York 2007), the luminosity is mainly arising from the high-mass stars inside the neighboring H II region.

The deconvolved (FWHM) size of MMS is  $(0''.53 \pm 0''.09) \times (0''.27 \pm 0''.06)$ , corresponding to  $\sim 2.2 \text{ pc} \times 1.1 \text{ pc}$ . The total mass of MMS ( $M_{\text{total}}^{\text{MMS}}$ ) above the  $3\sigma$  detection is estimated to be  $\sim 2 \times 10^4 M_\odot$  assuming the dust opacity of  $\kappa_{1.3\text{mm}}$  of  $1 \text{ cm}^2 \text{ g}^{-1}$  for protostellar envelopes (e.g., Ossenkopf & Henning 1994), a dust-to-gas ratio of  $\sim 3 \times 10^{-3}$  (for the LMC-like metallicity, Gordon et al. 2014), and the dust temperature of 20 K. The velocity width (FWHM) of the  $\text{C}^{18}\text{O}$  emission in MMS is  $6.8 \text{ km s}^{-1}$ . With a radius of 1.6 pc (=geometric mean of the major and minor axis) the resultant virial mass,  $\sim 2 \times 10^4 M_\odot$ , is consistent with the  $M_{\text{total}}^{\text{MMS}}$ , indicating that the dense clump is gravitationally bound. Assuming a spherical geometry, the average density of MMS is calculated to be  $\sim 2 \times 10^4 \text{ cm}^{-3}$ . We note that we could not find any other continuum sources as well as  $\text{C}^{18}\text{O}$  emission in the observed field, indicating that the high-density region is localized within a few pc with respect to the entire molecular cloud of GMC-16.

Figure 4 (d) shows spatial distributions of the high-velocity  $^{12}\text{CO}$  gas toward MMS. The spectra of  $^{12}\text{CO}$ ,  $^{13}\text{CO}$  and  $\text{C}^{18}\text{O}$  are shown in panels (e,f). The  $^{12}\text{CO}$  profile is slightly asymmetric with a peak velocity  $\sim -245 \text{ km s}^{-1}$ . As shown in the  $^{13}\text{CO}$  moment map in Figure 4 (b), there are two velocity components toward MMS, and the  $^{12}\text{CO}$  intensity of redshifted gas is stronger than that of the blueshifted gas. The double (or multiple) peaked profile in  $\text{C}^{18}\text{O}$  is insignificant at the present sensitivity. Since the  $^{13}\text{CO}$  profile shows a relatively symmetric shape, we use it to estimate the systemic velocity of MMS using Gaussian fitting. The systemic velocity judged from the  $^{13}\text{CO}$  profile is  $\sim -246 \text{ km s}^{-1}$  and the maximum relative velocity of the  $^{12}\text{CO}$  red/blueshifted wing components is  $\sim 20 \text{ km s}^{-1}$ . CO observations in the Galaxy and the LMC often found this type of high-velocity gas toward young stellar objects (e.g., Beuther et al. 2002; Fukui et al. 2015, 2019; Shimonishi et al. 2016; Harada et al. 2019; Tokuda et al. 2019). The presence of the gravitationally bound dense material toward MMS strongly indicate that there is at least one embedded high-mass protostar and the  $^{12}\text{CO}$  high-velocity components are originated from its bipolar outflow. This is the first strong candidate for protostellar outflow in M33 as well as the external disk galaxies. We further discuss the reliability of the protostellar outflow in Sect. 4.2.

## 4. DISCUSSIONS

### 4.1. Possible origins of the giant molecular filaments

We discuss the formation mechanism of the GMFs in GMC-16. Early molecular gas surveys in the Galaxy speculated that this type of long-filamentary structures is supposed to be formed by galactic spiral shocks (e.g., Burton, & Shane 1970; Jackson et al. 2010). Alternative ideas have also been proposed; for example, the streamer in W51 can be regarded as a part of the expansion ring based on its velocity structure (Moon, & Park 1998). Our extragalactic view of GMC-16 with a similar resolution of the Galactic single-dish studies allow us to address the origin of the GMFs. The morphology of the GMFs in GMC-16 shows a relatively straight shape, and the size of the H II regions are small compared to that of the GMFs. It is difficult to say that the GMFs are regarded as a part of the ring-like structure associated with the H II regions.

As shown in Sect. 3.1, we find clear position discrepancies between the GMFs and the H II regions. This type of spatial offset is sometimes seen in nearby grand-design spiral galaxies (Hirota et al. 2011; Colombo et al. 2014), although the separations are more than a few  $\times 10 \text{ pc}$ , which is much larger than the present case. The authors suggest that high-mass star formation activities are triggered by the density-wave driven galactic spiral shocks. The sequence of the GMFs and H II regions in GMC-16 is consistent with the propagation direction of the spiral arm. According to the steady-state density-wave theory (Lin, & Shu 1964), the interstellar medium is decelerated and compressed at the bottom of the stellar potential, i.e., shock front (Fujimoto 1968; Roberts 1969). If we adopt a rotation velocity of the interstellar medium,  $\sim 80 \text{ km s}^{-1}$  at 2 kpc from the galactic center (Corbelli et al. 2014), and a pattern speed,  $\Omega_p$ , of  $\sim 25 \text{ km s}^{-1} \text{ kpc}^{-1}$  (Newton 1980), the timescale of the propagation of the H II regions from the possible shock front traced by the CO filaments is calculated to be  $\sim 1 \text{ Myr}$  ( $= 20 \text{ pc} / (80 - 50) \text{ km s}^{-1}$ ) assuming that the GMFs and the H II regions are located at the same height in the galactic disk. This is consistent with the age of the H II regions judged from its sizes based on the Galactic studies (Tremblin et al. 2014). This means that the two major H II regions inside the observed field (Figure 2 (b)) might be formed around the present locations of Filament A/B, although the galactic shock alone may not be enough to trigger the high-mass star formation (see Sect. 4.3).

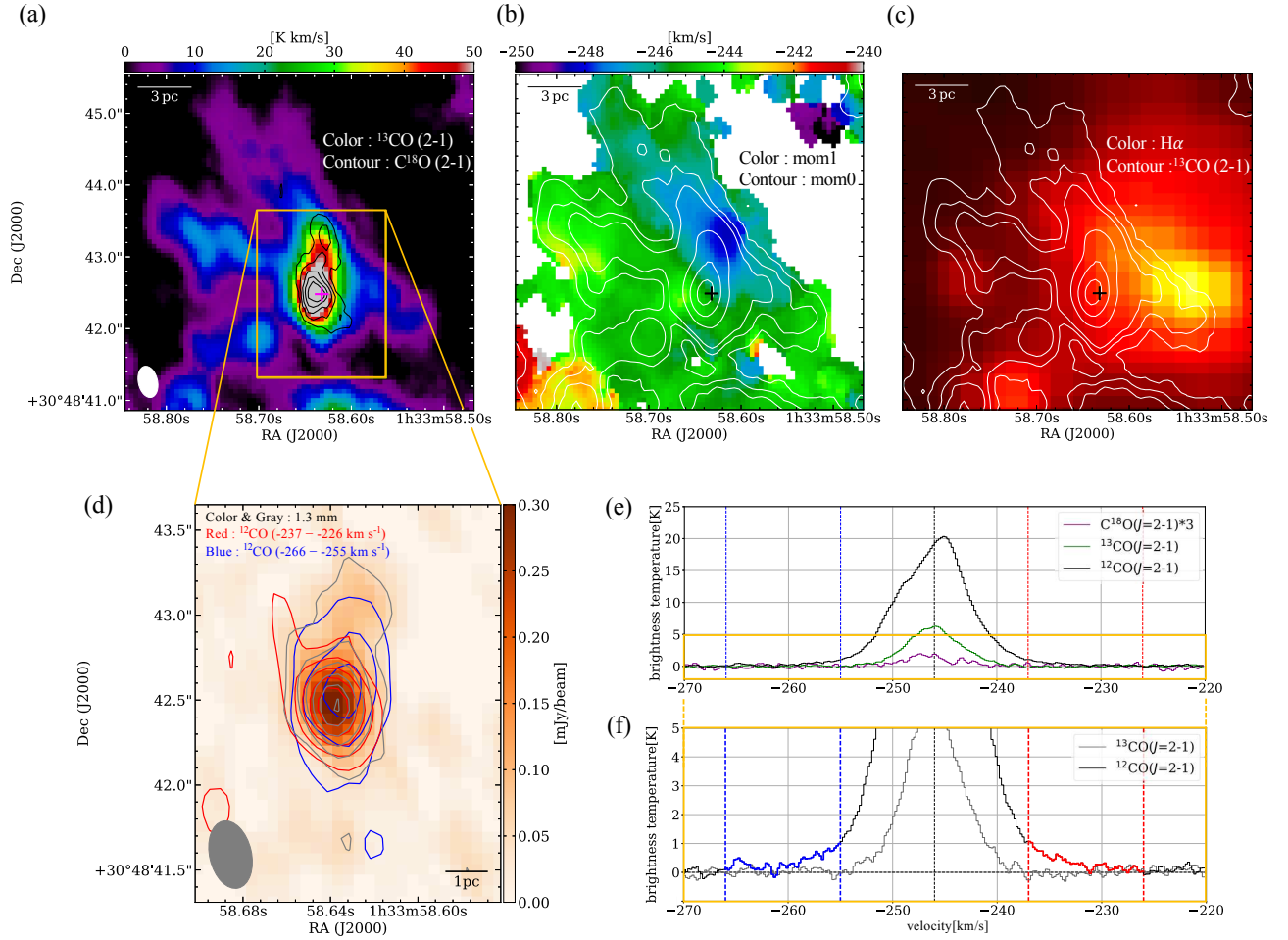


**Figure 4.** A dense clump associated with the  $^{12}\text{CO}$  bipolar outflow candidate in GMC-16. (a) Color-scale and black contours show the  $^{13}\text{CO}$  and  $\text{C}^{18}\text{O}$  velocity-integrated intensity maps, respectively. The lowest contour level and the subsequent contour steps are  $1.4 \text{ K km s}^{-1}$ . The cross denotes in panel (a,b,c) the peak position of MMS shown in panel (d). The angular resolution is given by the white ellipse in the lower left corner. (b) Color-scale image and white contours show the  $^{13}\text{CO}$  moment 1 map and moment 0 map, respectively. The lowest contour and the subsequent steps are the  $3\sigma$  noise level,  $2 \text{ K km s}^{-1}$ . (c) Color-scale image shows the  $\text{H}\alpha$  distributions. White contours are the same as panel (b). (d) Color-scale and gray contours show the 1.3 mm continuum emission. The lowest contour level and the subsequent steps are the  $3\sigma$  noise level,  $0.053 \text{ mJy beam}^{-1}$ . Red and blue contours represent the high-velocity  $^{12}\text{CO}$  emission originated from the outflowing gas. The integrated velocity ranges are shown in red and blue dotted lines in panel (e, f). The lowest contour and the subsequent steps are the  $3\sigma$  noise level,  $3.3 \text{ K km s}^{-1}$ . (e) The  $^{12}\text{CO}$ ,  $^{13}\text{CO}$ , and  $\text{C}^{18}\text{O}$  spectra at the peak position of MMS. Note that the  $^{12}\text{CO}$  data does not include the IRAM 30m data. The black dotted line indicates the central velocity,  $-246 \text{ km s}^{-1}$ , obtained by fitting the  $^{13}\text{CO}$  spectra with a single Gaussian profile. The velocity ranges of red and blue dotted lines are  $-237$  to  $-226 \text{ km s}^{-1}$ , and  $-266$  to  $-255 \text{ km s}^{-1}$ , respectively. (f) An enlarged view of the  $^{12}\text{CO}$  and  $^{13}\text{CO}$  profile in panel (e) to stress the wing feature of the outflowing gas.

We found a central velocity difference between the extended gas component ( $\sim -240 \text{ km s}^{-1}$ ) at the eastern (upstream) side of GMC-16 and the filamentary structures ( $\sim -245 \text{ km s}^{-1}$ ), as shown in Figure 3 and Sect. 3.1. Based on the  $\sim 40 \text{ pc}$  resolution measurements in CO and H I by Gratier et al. (2010), the velocity gradient along the north-south direction of the GMC is  $\lesssim 0.1 \text{ km s}^{-1} \text{ pc}^{-1}$ , which is mostly arising from the galactic rotation. The rotational motion alone may not simply explain the velocity offset ( $\sim 5 \text{ km s}^{-1}$ ) in the PV diagram (Figure 3(b)), which is extracted perpendicular to the large-scale gradient direction. In addition to this, the velocity width of the extended gas is larger than that of the filamentary clouds. These velocity features can be qualitatively explained by the dissipation of turbulent energy and deceleration of the gas at the shock front. The idea that filamentary structure can be seen as a consequence of turbulent dissipation has been proposed in various scales of interstellar medium (e.g., Padoan et al. 2001; Inoue et al. 2018; Tokuda et al. 2018). In addition to this, our observations toward GMC-8, which is a quiescent



GMC, shows less filamentary structures and a large velocity dispersion compared to the GMFs in GMC-16 (forthcoming paper). In summary, our indirect evidence suggests that the galactic spiral shock compresses a turbulent diffuse cloud to form filamentary structures.

In flocculent spiral galaxies like M33, it may be hard to realize strong spiral shocks compared to grand design galaxies (Egusa et al. 2011, 2017; Hirota et al. 2011; Colombo et al. 2014). Wada et al. (2011) proposed that the complex spiral structures found in M33 are explained by the non-steady stellar arms rather than the conventional density-wave picture. The galactic shear motion can elongate GMCs over  $\sim 100$  pc scale (Wada 2008; Miyamoto et al. 2014). The non-steady stellar arm model predicts that there is no clear spatial offset between gas spiral arm and young stars across the galaxy. Further statistical studies to investigate the position discrepancies between molecular clouds and H II regions based on observations toward similar targets in M33 with a similar angular resolution will allow us to draw a comprehensive picture of the relation between the galactic kinematics and GMF formation.

#### 4.2. High-velocity wing components as a strong candidate for protostellar outflow

We found the redshifted and blueshifted wing features at MMS (Sect. 3.2). According to the Galactic studies of high-mass star-forming regions (e.g., Beuther et al. 2002), such high-velocity wings with a maximum velocity of  $\sim \pm 20 \text{ km s}^{-1}$  or even much smaller velocities are normally interpreted as protostellar outflows. The typical size of outflow lobes in the Galaxy (e.g., Beuther et al. 2002) and the LMC (e.g., Fukui et al. 2019; Tokuda et al. 2019) is less than 1 pc. To demonstrate compactness of the possible outflow, we made the velocity profile maps around the MMS's location in  $^{12}\text{CO}$  and  $^{13}\text{CO}$  (Figure 5 in Appendix) with a grid size of  $0''.93 \times 0''.61$ , which corresponds to  $\sim 3.7 \text{ pc} \times \sim 2.5 \text{ pc}$ . We could not find similar high-velocity wing emission except the middle panel, i.e., at the location of MMS. These observational results strongly suggest that the high-velocity  $^{12}\text{CO}$  emission at MMS is a protostellar outflow.

We briefly mention the limitations of the present observations. As seen in Figure 4, there is no significant spatial offset between the red and blue velocity components. Because protostellar outflows are as compact as  $\lesssim 1$  pc as mentioned in the previous paragraph, this feature is mostly due to the lack of spatial resolution. For example, a low-resolution study toward the Galactic high-mass protostellar object AFGL 2591 identified the molecular outflow without a clear offset between the red and blueshifted components (Lada et al. 1984). Subsequently, Mitchell et al. (1991) clearly revealed its bipolar nature with a finer resolution measurement. A pole-on configuration is another possibility to interpret our data at MMS, in which case the accretion disk may be observable as face-on. However, the sizes of such disks associated with high-mass protostars are as small as  $\lesssim 1,000 \text{ au}$  (e.g., Motogi et al. 2019), which is much smaller than outflow lobes, and thus it is also impossible to resolve it with this measurement. The present elongation of MMS in the north-south direction is arising from the combination of the beam swelling effect and its filamentary nature.

Although we need much higher angular resolution observations to reveal the actual distribution of the outflow and its age, the current data tell us that the dynamical time ( $=\text{size}/\text{velocity}$ ) is as young as  $\sim (5-8) \times 10^4 \text{ yr}$  depending on the assumption of the inclination angle ( $45-60^\circ$ ). Considering the fact that the high-mass stars are frequently formed in binary or multiple manners (e.g., Massey 2003), MMS may be composed of unresolved multiple protostellar sources. Future high-resolution infrared and long-baseline ALMA observations will elucidate further detailed nature of the source.

#### 4.3. A possible trigger of the high-mass star formation in GMC-16

In Sect. 4.1, we suggest that the galactic shock may be a plausible mechanism to explain the GMF formation. However, the high-mass star-formation activity itself is localized within a few pc scales rather than the entire  $\sim 50$  pc scale filament. Although Filament B has a  $^{13}\text{CO}$  peak at the edge of the filament (Figure 1), we could not detect any dense gas tracers,  $\text{C}^{18}\text{O}$ , and 1.3 mm continuum so far. With respect to the H II regions, which represent the recent star formation activities (Figure 2 (b)), its distributions are discrete rather than continuous. These facts indicate that an additional factor may also be needed to trigger the high-mass star-formation.

One possible mechanism to trigger the high-mass star formation in MMS is “collect and collapse” (Elmegreen, & Lada 1977; Dale et al. 2007) driven by the expansion of the nearby H II region (Figure 4 (c)). However, the velocity gradient traced by the  $^{13}\text{CO}$  emission (Figure 4 (b)) does not follow the direction of the expanding motion judged from the distribution of the H II region. It is unlikely that the second generation star formation in MMS of GMC-16 was triggered by the expanding motion.

The moment 1 map shows a drastic velocity change at the boundary between the northern and eastern filaments as mentioned in Sect. 3.2. This type of velocity difference is often seen in high-mass star-forming filamentary clouds

in the LMC at a sub-pc resolution (Fukui et al. 2015; Saigo et al. 2017; Harada et al. 2019; Nayak et al. 2019), and its interpretation is that collision between two or several filaments trigger high-mass star formation. More recently, the follow-up observations toward some of the targets with a spatial resolution of  $\lesssim 0.1$  pc resolved further complex substructures composed of many filaments, which are difficult to explain by a coalescence process of individual components (Fukui et al. 2019; Tokuda et al. 2019). Nevertheless, because the orientation of filaments in the two different high-mass star-forming regions separated by over 50 pc is roughly aligned, they concluded that a tidally driven galactic-scale colliding flow (see, Fukui et al. 2017; Tsuge et al. 2019) induced the formation of the fan-shaped hub filaments as precursors of high-mass stars following the propagation direction of the flow. Such a hub filament is also reproduced by numerical simulations of cloud–cloud collision (Inoue et al. 2018).

In GMC-16, as shown in Figure 4 (a,b,c), the hub-filamentary structure extends toward the eastern direction, which is considered to be the upstream side in the spiral shock. Although the large-scale spiral shock may form the GMFs with a length of  $\gtrsim 50$  pc as discussed in the Sect. 4.1, the formation of the small-scale hub filament may not be explained by the spiral shock alone. An additional factor, such as a collision between the GMF and a pre-existing small cloud, is needed to interpret the localization of the hub-filamentary dense clump leading to high-mass star formation. We note that similar hub-like molecular complex is also found in NGC 604-GMC (K., Muraoka et al. 2020 in preparation). According to the galactic scale numerical simulations, cloud–cloud collisions frequently occur around the galactic potential where interstellar media are concentrated (e.g., Dobbs, & Baba 2014). Sano et al. (2019) found a high-mass star-forming clump possibly formed by a collision between two clouds in the central region in M33, suggesting that cloud–cloud collision is not a rare event in M33 (see also, Tachihara et al. 2018; K., Muraoka et al. 2020 in preparation). The Galactic high-mass star-forming regions NGC 6334 and NGC 6357 (Persi & Tapia 2008) are also good counterparts to consider the high-mass star formation activities analogous to GMC-16. The regions contain several bright infrared sources with a total luminosity of  $>10^5 L_\odot$  along the molecular filament with a length of  $\sim 100$  pc. Fukui et al. (2018) concluded that a cloud–cloud collision promoted over a 100 pc scale mini-starburst in the NGC 6334 and NGC 6357 regions. Our GMC-16 studies may be equivalent to observations of such Galactic high-mass star-forming regions from outside the Galaxy.

## 5. SUMMARY

We have performed ALMA observations toward one of the most massive GMCs in M33, GMC-16, associated with a few H II regions. The spatial resolution is  $\sim 1$  pc, which is the highest angular resolution molecular gas survey in M33 (see also K., Muraoka et al. 2020 in preparation). We have spatially resolved  $>50$  pc scale giant molecular filaments (GMFs) with a mass of  $\sim 10^5 M_\odot$  along with the spiral arm in M33. One of the most striking features is a  $\sim 10$ – $20$  pc scale offset between the GMFs and H II regions, suggesting that the density-wave driven galactic shock may convert the diffuse interstellar gas into the filamentary structures and promote the subsequent high-mass star formation. At the southern part of the GMC, the 1.3 mm continuum and  $C^{18}O$  observations have found a  $\sim 1$  pc scale dense clump (MMS) with an average number density of  $\sim 10^4 \text{ cm}^{-3}$  at the intersection of the hub-filamentary cloud possibly formed by a cloud–cloud collision. We found a promising candidate for protostellar outflow at one of the GMFs, indicating that high-mass star-formation is still ongoing in MMS.

## ACKNOWLEDGMENTS

This paper makes use of the following ALMA data: ADS/ JAO.ALMA#2017.1.00461.S. ALMA is a partnership of the ESO, NSF, NINS, NRC, NSC, and ASIAA. The Joint ALMA Observatory is operated by the ESO, AUI/NRAO, and NAOJ. This work was supported by NAOJ ALMA Scientific Research Grant Numbers 2016-03B and JSPS KAKENHI (Grant Nos. 17K14251, 18K13582, 18K13587, and 18H05440).

*Software:* CASA (v5.4.0; McMullin et al. 2007), Astropy (Astropy Collaboration et al. 2018), APLpy (Robitaille & Bressert 2012)

## APPENDIX

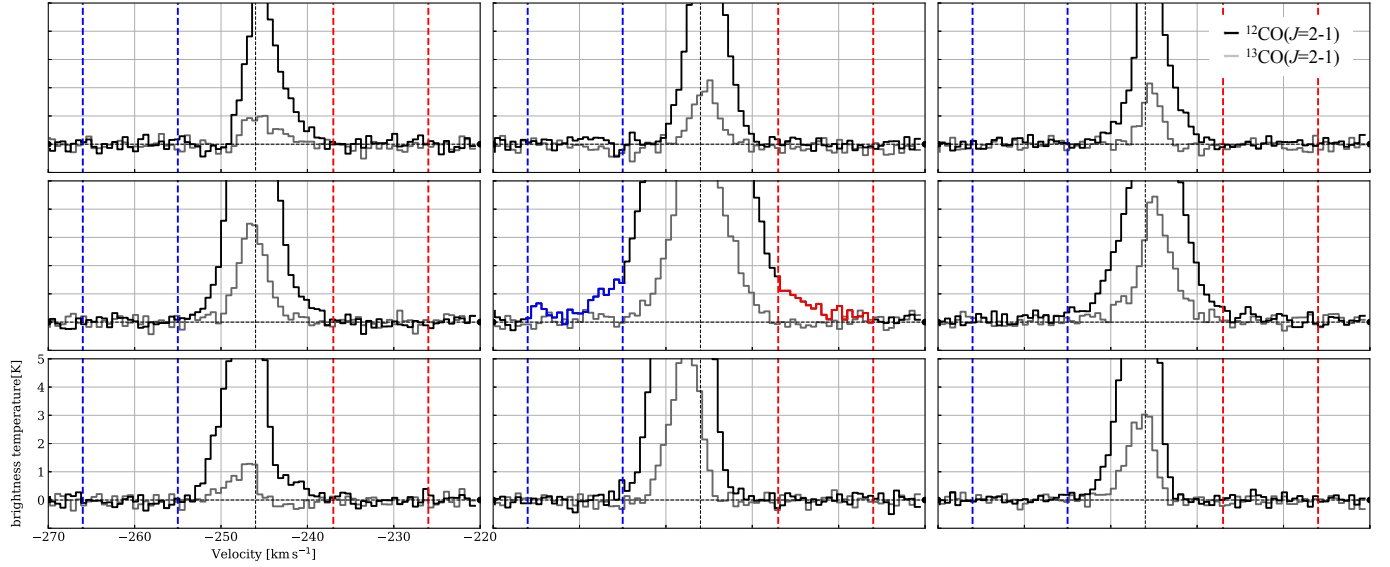


**Figure 5.** Velocity profile maps in  $^{12}\text{CO}$  and  $^{13}\text{CO}$  centered at the position of MMS. The black, blue, and red dotted lines are the same as in Figure 4 (e,f).

## REFERENCES

- André, P., Di Francesco, J., Ward-Thompson, D., et al. 2014, in *Protostars and Planets VI*, ed. H. Beuther et al. (Tucson, AZ: Univ. Arizona Press), 27
- André, P., Revéret, V., Könyves, V., et al. 2016, *A&A*, 592, A54
- Astropy Collaboration, Price-Whelan, A. M., Sipőcz, B. M., et al. 2018, *AJ*, 156, 123
- Arzoumanian, D., André, P., Didelonet, P. et al. 2011, *A&A*, 529, L6
- Arzoumanian, D., André, P., Könyves, V., et al. 2019, *A&A*, 621, A42
- Bailer-Jones, C. A. L., Rybizki, J., Fouesneau, M., et al. 2018, *AJ*, 156, 58
- Beuther, H., Schilke, P., Sridharan, T. K., et al. 2002, *A&A*, 383, 892
- Burton, W. B., & Shane, W. W. 1970, *The Spiral Structure of Our Galaxy*, 397
- Colombo, D., Meidt, S. E., Schinnerer, E., et al. 2014, *ApJ*, 784, 4
- Corbelli, E., Braine, J., Bandiera, R., et al. 2017, *A&A*, 601, A146
- Corbelli, E., & Salucci, P. 2000, *MNRAS*, 311, 441
- Corbelli, E., Thilker, D., Zibetti, S., et al. 2014, *A&A*, 572, A23
- Dale, J. E., Bonnell, I. A., & Whitworth, A. P. 2007, *MNRAS*, 375, 1291
- Dobbs, C., & Baba, J. 2014, *PASA*, 31, e035
- Druard, C., Braine, J., Schuster, K. F., et al. 2014, *A&A*, 567, A118
- Egusa, F., Koda, J., & Scoville, N. 2011, *ApJ*, 726, 85
- Egusa, F., Mentuch Cooper, E., Koda, J., & Baba, J. 2017, *MNRAS*, 465,
- Egusa, F., Sofue, Y., & Nakanishi, H. 2004, *PASJ*, 56, L45460
- Elmegreen, B. G., & Lada, C. J. 1977, *ApJ*, 214, 725
- Frerking, M. A., Langer, W. D., & Wilson, R. W. 1982, *ApJ*, 262, 590
- Freedman, W. L., Madore, B. F., Gibson, B. K., et al. 2001, *ApJ*, 553, 47
- Fujii, K., Minamidani, T., Mizuno, N., et al. 2014, *ApJ*, 796, 123
- Fujimoto, M. 1968, *Non-stable Phenomena in Galaxies*, 453
- Fujita, S., Torii, K., Kuno, N., et al. 2019, *PASJ*,
- Fukui, Y., Mizuno, N., Yamaguchi, R., et al. 1999, *PASJ*, 51, 745
- Fukui, Y., Harada, R., Tokuda, K., et al. 2015, *ApJ*, 807, L4
- Fukui, Y., Kohno, M., Yokoyama, K., et al. 2018, *PASJ*, 70, S41



- Fukui, Y., Tokuda, K., Saigo, K., et al. 2019, *ApJ*, 886, 14
- Fukui, Y., Tsuge, K., Sano, H., et al. 2017, *PASJ*, 69, L5
- Goldsmith, P. F., Heyer, M., Narayanan, G., et al. 2008, *ApJ*, 680, 428
- Gordon, K. D., Roman-Duval, J., Bot, C., et al. 2014, *ApJ*, 797, 85
- Gratier, P., Braine, J., Rodriguez-Fernandez, N. J., et al. 2010, *A&A*, 522, A3
- Hacar, A., Tafalla, M., Kauffmann, J., et al. 2013, *A&A*, 554, A55
- Harada, R., Onishi, T., Tokuda, K., et al. 2019, *PASJ*, 71, 44
- Heyer, M., & Dame, T. M. 2015, *ARA&A*, 53, 583
- Hirota, A., Kuno, N., Sato, N., et al. 2011, *ApJ*, 737, 40
- Inoue, T., Hennebelle, P., Fukui, Y., et al. 2018, *PASJ*, 70, S53
- Jackson, J. M., Finn, S. C., Chambers, E. T., et al. 2010, *ApJL*, 719, L185
- Lada, C. J., Thronson, H. A., Smith, H. A., et al. 1984, *ApJ*, 286, 302
- Lin, C. C., & Shu, F. H. 1964, *ApJ*, 140, 646
- Kawamura, A., Mizuno, Y., Minamidani, T., et al. 2009, *ApJS*, 184, 1
- Kepley, A. A., Tsutsumi, T., Brogan, C. L., et al. 2020, *PASP*, 132, 024505
- Koo, B.-C. 1999, *ApJ*, 518, 760
- Martins, F., Schaerer, D., & Hillier, D. J. 2005, *A&A*, 436, 1049
- Massey, P. 2003, *ARA&A*, 41, 15
- McMullin, J. P., Waters, B., Schiebel, D., et al. 2007, *Astronomical Data Analysis Software and Systems XVI*, 127
- Miura, R. E., Kohno, K., Tosaki, T., et al. 2012, *ApJ*, 761, 37
- Mitchell, G. F., Maillard, J.-P., & Hasegawa, T. I. 1991, *ApJ*, 371, 342
- Miyamoto, Y., Nakai, N., & Kuno, N. 2014, *PASJ*, 66, 36
- Mizuno, A., Onishi, T., Yonekura, Y., et al. 1995, *ApJL*, 445, L161
- Moon, D.-S., & Park, Y.-S. 1998, *MNRAS*, 296, 863
- Motogi, K., Hirota, T., Machida, M. N., et al. 2019, *ApJL*, 877, L25
- Myers, P. C. 2009, *ApJ*, 700, 1609
- Nayak, O., Meixner, M., Sewilo, M., et al. 2019, *ApJ*, 877, 135
- Newton, K. 1980, *MNRAS*, 190, 689
- Okumura, S.-I., Miyawaki, R., Sorai, K., et al. 2001, *PASJ*, 53, 793
- Onishi, T., Mizuno, A., Kawamura, A., Ogawa, H., & Fukui, Y. 1996, *ApJ*, 465, 815
- Onodera, S., Kuno, N., Tosaki, T., et al. 2010, *ApJL*, 722, L127
- Ossenkopf, V., & Henning, T. 1994, *A&A*, 291, 943
- Padoan, P., Juvela, M., Goodman, A. et al. 2001, *ApJ*, 553, 227
- Peretto, N., Fuller, G. A., Duarte-Cabral, A., et al. 2013, *A&A*, 555, A112
- Persi, P., & Tapia, M. 2008, *Handbook of Star Forming Regions*, Volume II, 5, 456
- Roberts, W. W. 1969, *ApJ*, 158, 123
- Robitaille, T., & Bressert, E. 2012, *APLpy: Astronomical Plotting Library in Python*, ascl:1208.017
- Rosolowsky, E., Keto, E., Matsushita, S., & Willner, S. P. 2007, *ApJ*, 661, 830
- Saigo, K., Onishi, T., Nayak, O., et al. 2017, *ApJ*, 835, 108
- Sandage, A., & Humphreys, R. M. 1980, *ApJ*, 236, L1
- Sano, H., Tsuge, K., Tokuda, K., et al. 2019, *arXiv e-prints*, arXiv:1908.08404
- Sawada, T., Koda, J., & Hasegawa, T. 2018, *ApJ*, 867, 166
- Shimonishi, T., Onaka, T., Kawamura, A., et al. 2016, *ApJ*, 827, 72
- Shu, F. H., Milione, V., & Roberts, W. W. 1973, *ApJ*, 183, 819
- Tachihara, K., Gratier, P., Sano, H., et al. 2018, *PASJ*, 70, S52
- Tokuda, K., Fukui, Y., Harada, R., et al. 2019, *ApJ*, 886, 15
- Tokuda, K., Onishi, T., Saigo, K. et al. 2018, *ApJ*, 826, 8
- Torii, K., Fujita, S., Nishimura, A., et al. 2019, *PASJ*, 50
- Tosaki, T., Kuno, N., Onodera, S. M., et al. 2011, *PASJ*, 63, 1171
- Tremblin, P., Anderson, L. D., Didelon, P., et al. 2014, *A&A*, 568, A4
- Tsuge, K., Sano, H., Tachihara, K., et al. 2019, *ApJ*, 871, 44
- Verley, S., Hunt, L. K., Corbelli, E., et al. 2007, *A&A*, 476, 1161
- Wada, K. 2008, *ApJ*, 675, 188
- Wada, K., Baba, J., & Saitoh, T. R. 2011, *ApJ*, 735, 1
- Wong, T., Hughes, A., Ott, J., et al. 2011, *ApJS*, 197, 16
- Wong, T., Hughes, A., Tokuda, K., et al. 2019, *ApJ*, 885, 50
- Williams, G. M., Peretto, N., Avison, A., Duarte-Cabral, A., & Fuller, G. A. 2018, *A&A*, 613, A11
- Zinnecker, H., & Yorke, H. W. 2007, *ARA&A*, 45, 481